

X-RAY STUDIES OF BLAZAR 1ES 1959+650 USING SWIFT & XMM-NEWTON SATELLITE

KIRAN A WANI^{1,2}, HARITMA GAUR¹ AND M K PATIL²*Draft version May 8, 2023*

ABSTRACT

High synchrotron energy peaked blazar 1ES 1959+650 is studied with Swift and XMM-Newton satellite in total 127 observations during the period June 2018–December 2020. We extensively studied its flux and spectral variability on intra-day and long-term timescales. Discrete correlation function analysis between soft and hard X-ray bands indicates soft as well as hard lags. The results are used to constrain the magnetic field of the emitting region which is found to be 0.64 ± 0.05 Gauss. On long-term timescales, distribution of fluxes shows lognormality behaviour which could be attributed to minijets-in-a-jet model or might be due to the propagation of relativistic shocks down the jet. The spectral energy distribution around the synchrotron peak is well described by the log parabola model. Spectral parameters like peak energy E_p , curvature β and the peak luminosity L_p are derived from spectral analysis. Their correlations are studied to constrain the acceleration processes of the emitting particles. E_p shows strong correlation with L_p during the high state of the source which indicates spectral changes might be caused by the variations of the average electron energy. Low values of curvature parameter β and a weak correlation between E_p and β indicates co-existence of stochastic/statistical acceleration of electrons in the emitting region. Implications of other results are also discussed.

Subject headings: radiation mechanisms: non-thermal – galaxies: active – galaxies

1. INTRODUCTION

Blazar, a subclass of AGN, constitutes BL Lacertae objects (BL Lacs) and flat spectrum radio quasars (FSRQs). Blazars are characterized by rapid flux variability at time scales ranging from a few minutes to years across the entire electromagnetic spectrum; high optical polarisation and the emission is predominantly non-thermal in nature which emanates from a relativistic jet streaming along or aligned very close to our line of sight (Blandford & Rees 1978).

The spectral energy distribution of blazars consists of double peaked hump with the first one peaking in sub-mm to soft X-rays, whereas the second hump peaks at MeV to TeV energies (Urry & Padovani 1995). The low energy component of the SED is mostly due to the synchrotron emission from the relativistic electrons. However, the physical mechanisms behind the high energy emission are not well understood and are thought to be originating from the Compton upscattering of synchrotron photons by same population of relativistic electrons (Synchrotron self Compton, SSC i.e. Ghisellini & Maraschi 1989; Mastichiadis & Kirk 1997) or external seed photons originating from the accretion disc, broad line region (BLR) and torus components of a blazar (External Compton, EC i.e. Dermer et al. 1992; Ghisellini et al. 1998). The other models which appear to be viable mechanisms to explain the X-ray through γ -ray emission are hadronic models where the high energy emis-

sion is produced by relativistic protons through proton synchrotron radiation and photo-pion production, followed by pion decay and electromagnetic cascades (e.g. Mannheim & Biermann 1992; Böttcher et al. 2013, and references therein).

Blazars are divided into three classes based on the position of synchrotron peak in their SED (Padovani & Giommi 1995). Low frequency BL Lac objects exhibit synchrotron peak in IR-Optical band, intermediate frequency BL Lac objects have their synchrotron peak at optical-UV frequencies and high frequency BL Lac (HBL) objects show a synchrotron peak in the UV to X-ray band.

1ES 1959+650 is at a redshift of $z=0.048$ (Perlman et al. 1996) and is a prominent high synchrotron peaked blazar in which the synchrotron peak of the SED appears in the UV-X-ray band (Krawczynski et al. 2004; Kapanadze et al. 2016b; Abdo et al. 2010). In X-rays, it was first detected by the Slew Survey with the Einstein Imaging Proportional Counter (IPC) (i.e. Elvis et al. 1992), followed by BeppoSAX (Beckmann et al. 2002), RXTE, Swift, XMM-Newton (Tagliaferri et al. 2003; Massaro et al. 2008), by the Nuclear Spectroscopic Telescope Array (NuSTAR) (Pandey et al. 2017) in later years.

It has shown strong flux variability in optical, X-ray and TeV energy bands (i.e. Krawczynski et al. 2004; Kapanadze et al. 2016b, 2018a,b; Kaur et al. 2017; Patel et al. 2018; Wang et al. 2018, 2019; MAGIC Collaboration et al. 2020). High X-ray flaring activity of the source has been reported by Perlman et al. (2005) and Krawczynski et al. (2004) using XMM-Newton and RXTE-PCA observations in 2002–2003. Kapanadze et al. (2016b) reported frequent X-ray flares of this source

¹ Aryabhata Research Institute of Observational Sciences (ARIES), Manora Peak, Nainital - 263 002, India; harry.gaur31@gmail.com; kiranwani189@gmail.com

² School of Physical Sciences, SRTM University, Nanded, 431 606, India

during 2005–2014 using Swift–XRT observations.

1ES 1959+650 underwent an unprecedented X-ray flaring activity during August 2015–January 2016. During this period, it varied by a factor of ~ 5.7 with maximum value above 20 counts/sec, along with high flux activity in TeV energy band (i.e. Kapanadze et al. 2016b; Kaur et al. 2017; Patel et al. 2018). However, in several multi-wavelength campaigns, orphan flares in γ -rays (which are not simultaneous with X-ray flares) have been found in June 2002 (i.e. Krawczynski et al. 2004) and found that the orphan γ -ray flare cannot be explained with conventional one-zone SSC models. They invoked Multiple-Component SSC models; External Compton models where the variations of the external photon intensity in the jet frame can cause orphan γ -ray flares; magnetic field aligned along jet axis and thus the observer would not see the synchrotron flare but the electrons would scatter SSC γ -rays in our direction and thus be able to see the inverse Compton flare. Böttcher (2005) proposed that orphan flares are difficult to reconcile with the standard leptonic SSC model and suggested that they may originate from relativistic protons interacting with an external photon field supplied by electron synchrotron radiation reflected off a dilute reflector. Chandra et al. (2021) modelled the SED of this blazar using a single zone time dependent SSC model which could explain the flares successfully. Patel et al. (2018) studied this source during observation period June–July 2016 and explained its broadband SED using two zone SSC model where the inner zone is mainly responsible for producing the synchrotron peak and the high energy γ -ray part whereas, the second zone explains less variable optical-UV and low energy γ -ray emission.

The X-ray spectral index hardens with increasing flux level in the long-term duration (Patel et al. 2018; MAGIC Collaboration et al. 2020). and also during a number of flares (i.e. Wang et al. 2018). Kapanadze et al. (2016b, 2018b,a) also showed the ‘harder-when- brighter’ trend in blazar 1ES 1959+650. Recently, Chandra et al. (2021) presented an extensive analysis of 1ES 1959+650 during the period 2016–2017, until February 2021 using the X-ray data from AstroSAT and Swift and found that the synchrotron peak shifts significantly with different flux states. Shah et al. (2021) also used AstroSAT observations to study the anti-correlation between the photon index and the X-ray flux using a broken power law.

Around the synchrotron peak, SED is curved and can be well described by log parabolic model (e.g. Landau et al. 1986; Massaro et al. 2004; Tramacere et al. 2007; Chen 2014; Gaur et al. 2018; Pandey et al. 2018)). It is characterized by the peak energy (E_p), peak luminosity (L_p) and the curvature parameter β . The log parabolic spectral distribution arises when the acceleration probability is a decreasing function of electron energy. By analyzing large X-ray observations, it is suggested by Massaro et al. (2004); Tramacere et al. (2007, 2011) that the observed anti-correlation expected between E_p and β could be used as a signature of a stochastic component in the acceleration process. For the blazar population, an apparent anti-correlation is expected between E_p and L_p (e.g. Tramacere et al. 2007; Massaro et al. 2008; Kapanadze et al. 2016b, 2017, 2018a) which might

be associated with the change in average electron energy, beaming factor or magnetic field (e.g. Tramacere et al. 2009).

In the present work, we analyzed Swift observations of 1ES 1959+650 during the period June 2018–December 2020 in 125 nights. We also studied two XMM–Newton satellite observations available during this period. Our aim is to study the temporal/spectral variability of this source on timescales from minutes to years covering different flux states. Studying flux and spectral variability during different flux states are important as distinct physical processes may play a dominant role in different flux states. Flux and spectral variations of blazars on diverse timescales arises either due to pure intrinsic phenomenon such as the interaction of relativistic shocks with particle density or magnetic field irregularities in the jet (e.g. Marscher 2014); production of minijets-in-a-jet (e.g. Giannios et al. 2009) or due to extrinsic mechanisms. Extrinsic mechanisms involve the geometrical effects that results due to bending of the jets, either through instabilities (e.g. Pollack et al. 2016) or through orbital motion (e.g. Fromm et al. 2013; Larionov et al. 2020; Valtonen & Wiik 2012). Long term variability is generally attributed to a mixture of intrinsic as well as extrinsic mechanisms which includes shocks propagating down twisted jets or relativistic plasma blobs moving downstream helical structure in the magnetized jets (e.g. Marscher et al. 2008). Spectral energy distribution of blazars are explained by leptonic and hadronic models (Böttcher et al. 2013) and flux and spectral variability can be explained by merely changing the SED parameters adopting a common set of physical mechanisms (e.g. Patel et al. 2018; Prince et al. 2019; Ghosal et al. 2022). We fit the spectra using log parabolic model and derived spectral parameters i.e. E_p , L_p and β which varies with different flux states of the source. In this work, we analyzed correlations between these spectral parameters during different flux states of the source which could provide tight observational constraints upon the acceleration and injection processes of the emitting electrons.

The paper is structured as follows. Section 2 describes observation and data analysis procedures of Swift and XMM–Newton satellites. Section 3 provides the analysis techniques used to quantify variability, variability timescales and power spectral density. Section 4 provides the spectral analysis and various models used in the studies. In section 5, we describe the results and their interpretation. Results are discussed and summarized in section 6.

2. DATA REDUCTION AND ANALYSIS

2.1. SWIFT

Neil Gehrels Swift observatory is a multi-wavelength facility equipped with X-ray Telescope (XRT), the Burst Alert Telescope (BAT) and Ultraviolet/ Optical Telescope (UVOT) (Gehrels et al. 2004). We retrieved the Swift–XRT (Burrows et al. 2005) data from publicly available HEASARC data archive. The data reduction is performed with the XRT Data Analysis Software (v.3.6.0) which is a part of the HEASoft package (v.6.28). Level 1 unscreened event files were reduced, calibrated and cleaned with the use of XRTPipeline script (ver-

TABLE 1
OBSERVATION LOG OF XMM-NEWTON AND SWIFT-XRT DATA FOR
BLAZAR 1ES 1959+650.

Satellite	Date (yyyy mm dd) (Observation ID)	Exposure Time (sec)	F_{var} (%)	
XMM-Newton	2019-07-05 (0850980101)	42139.94	1.95 ± 0.07	
	2020-07-16 (0870210101)	31239.34	3.12 ± 0.09	
	2018-06-03 (00094153007)	1007.94	-	
Swift-XRT	2018-06-10 (00094153008)	988.12	1.80 ± 2.03	
	2018-06-10 (00034588142)	1002.94	1.39 ± 2.74	
	2018-06-14 (00034588143)	1003.10	-	

#Complete table of all observations appear in online supplementary material

sion 0.13.5). Latest calibration files of Swift CALDB are used with remote access³. All the observations are in Windowed Timing mode. Events are selected with standard filtering criteria of 0-2 grades for Windowed Timing (WT) observations. The sources with its centre pixels lying inside the two pixel radius of bad pixels are not used in the analysis. Source region is extracted with a circular region of 20 pixel radius. For the Windowed timing mode, the source should appear in the middle of the 1-D image, therefore the background can be selected in regions on either side of the source.

XRTPRODUCTS is used to obtain the light curve and spectrum of the source and background. The obtained source light curve is corrected for the resultant loss of effective area, bad/hot pixels and vignetting with the use of XRTLCCORR task. The ancillary response files (ARFs) were created using the XRTMKARF task. Source spectra were binned to ensure at least 20 count per bin in order to use the χ^2 fitting method.

2.2. XMM-Newton

Blazar 1ES 1959+650 is observed on 5th July 2019 and 16th July 2020 by XMM-Newton satellite (Jansen et al. 2001). We used the European Photon Imaging Camera (EPIC) pn instrument data. EPIC-pn is most sensitive and less affected by the photon pile-up effects (Strüder et al. 2001). Data reduction is performed with the use of XMM-Newton Science Analysis System (SAS) for the LC extraction. We extracted the high energy (10 keV < E < 12 keV) light curve for the full frame of the exposed CCD in order to identify flaring particle background. We restrict our analysis to the 0.3–10 keV energy range, as data below 0.3 keV are markedly contaminated by noise events and data above 10 keV are usually dominated by background flares. Source region is extracted using a circle of 40 arcsec radius centered on the source. Background light curve is obtained from the region that corresponds to circular annulus centered on the source with inner and outer radius of 50 arcsec and 60 arcsec, respectively. Pile up effect is examined using the SAS task EPATPLOT. We found a pile-up in our observations. In order to remove the pile-up, the central 7.5 arcsec radius region is removed while extracting the

LC. Source LCs are obtained for the 0.3-10 keV energy band (corrected for background flux and given in units of counts s⁻¹), sampled with a fixed bin size of 0.5 ks.

3. ANALYSIS TECHNIQUES

3.1. Excess Variance

Excess variance (σ_{XCS}^2) is a measure of source intrinsic variance (Edelson et al. 2002; Vaughan et al. 2003a) evaluated by subtracting the variance that arises from measurement errors ($\bar{\sigma}_{err}^2$) from the total variance of the observed LC (S^2). If a LC consists of N measured flux values x_i with corresponding finite uncertainties $\sigma_{err,i}$ arising from measurement errors, then the normalised excess variance (σ_{NXS}^2) is calculated as follows:

$$\sigma_{NXS}^2 = \frac{S^2 - \bar{\sigma}_{err}^2}{\bar{x}^2}, \quad (1)$$

where \bar{x} is the arithmetic mean of x_i , $\bar{\sigma}_{err}^2 = \frac{1}{N} \sum_i \sigma_{err,i}^2$ is the mean square error and S^2 is the sample variance of the LC, as given by

$$S^2 = \frac{1}{N-1} \sum_i (x_i - \bar{x})^2. \quad (2)$$

The fractional rms variability amplitude, F_{var} (Edelson et al. 1990; Rodríguez-Pascual et al. 1997), which is the square root of σ_{NXS}^2 is thus

$$F_{var} = \sqrt{\frac{S^2 - \bar{\sigma}_{err}^2}{\bar{x}^2}}. \quad (3)$$

The uncertainty on F_{var} is given by (Vaughan et al. 2003a).

$$err(F_{var}) = \sqrt{\left(\sqrt{\frac{1}{2N}} \frac{\bar{\sigma}_{err}}{\bar{x}^2 F_{var}}\right)^2 + \left(\sqrt{\frac{\bar{\sigma}_{err}^2}{N}} \frac{1}{\bar{x}}\right)^2}. \quad (4)$$

3.2. Hardness Ratio

Hardness ratio (HR) is useful to characterise the spectral changes over a broad X-ray energy range (e.g. Park et al. 2006; Sivakoff et al. 2004). The energy range of (0.3–2) keV and (2–10) keV are used here as soft and hard bands respectively. Hardness ratio is then defined as:

$$HR = \frac{(H - S)}{(H + S)}, \quad (5)$$

and the error in HR (σ_{HR}) is calculated, as follows:

$$\sigma_{HR} = \frac{2}{(H + S)^2} \sqrt{S^2 \sigma_H^2 + H^2 \sigma_S^2}, \quad (6)$$

where S and H are the net count rates in the soft (0.3–2 keV) and hard (2–10 keV) bands, respectively, while σ_S and σ_H are their respective errors (e.g. Pandey et al. 2017).

³ <https://heasarc.gsfc.nasa.gov/FTP/caldb>

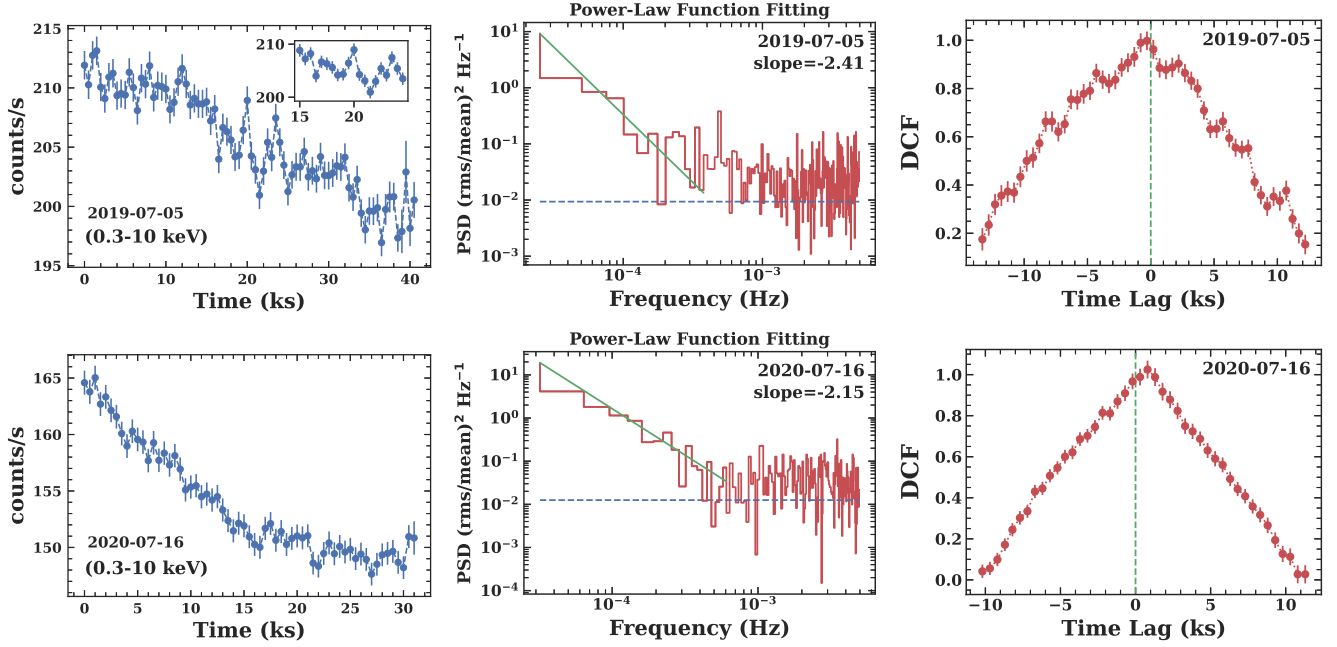


FIG. 1.— XMM-Newton light curves with their corresponding PSD and DCF of Blazar 1ES 1959+650. DCF is performed between X-ray energy range of 0.3-2 keV (soft band) and 2-10 keV (hard band). PSD is performed in the X-ray energy range of 0.3–10 keV.

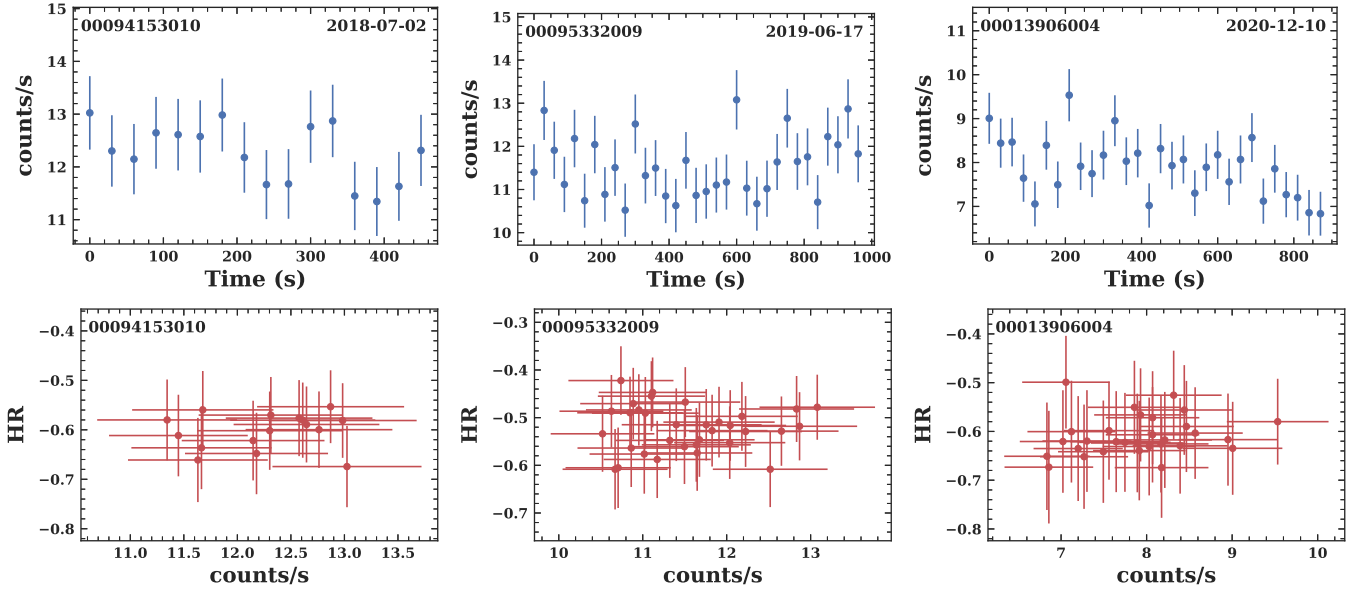


FIG. 2.— Sample of Swift-XRT light curves and their corresponding plot of HR versus counts/s. Hardness Ratio (HR) is calculated between the X-ray energy range of 0.3-2 keV (soft band) and 2-10 keV (hard band). Complete set of light curves of all Swift observations (139 images) appears in a figure set in the online Journal.

3.3. Doubling/Halving Timescales

Characteristic halving/doubling timescale τ , depending on the increase or decrease in the flux, is the shortest flux variability time which is calculated from:

$$F(t_1) = F(t_2) 2^{(t_1-t_2)/\tau_{var}}, \quad (7)$$

where $F(t_1)$ and $F(t_2)$ are the fluxes of the LC at times t_1 and t_2 , respectively. We consider the timescales when the difference in flux is significant at 3σ level (e.g. Foschini et al. 2011; Dhiman et al. 2021).

3.4. Discrete Correlation Function

Discrete correlation function is calculated for light curves of two different energy bands. We consider here 0.3-2 keV and 2-10 keV as two energy bands. It is used to investigate a correlation between two unevenly sampled time series data. For such two discrete data sets a_i and b_j , unbinned discrete correlation is defined as (Edelson & Krolik 1988):

$$UDCF_{ij} = \frac{(a_i - \bar{a})(b_j - \bar{b})}{\sqrt{(\sigma_a^2 - e_a^2)(\sigma_b^2 - e_b^2)}}, \quad (8)$$

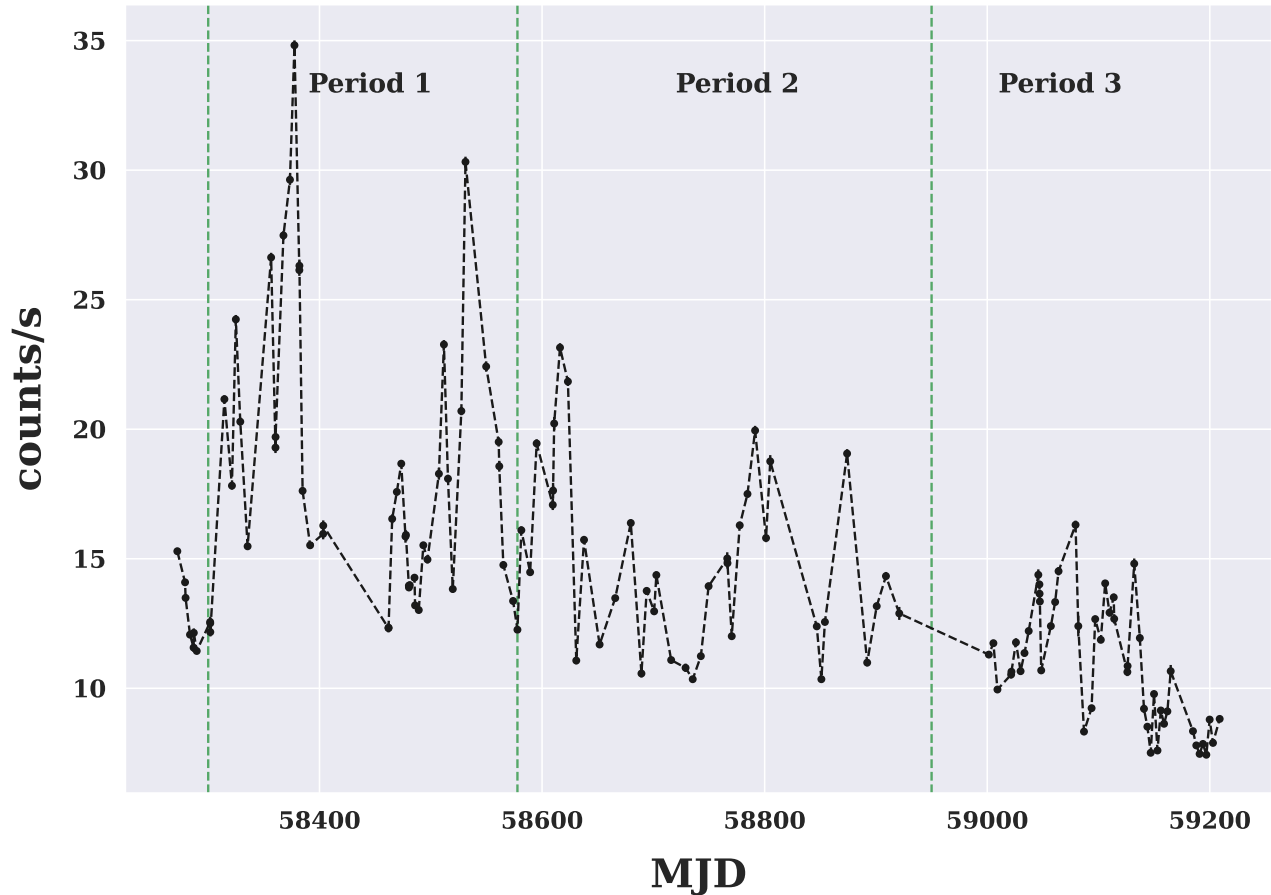


FIG. 3.— Long term light curve of blazar 1ES 1959+650 using Swift-XRT observations from June 2018 to December 2020. Vertical green dashed line separates the three periods considered for the analysis. Period 1 corresponds to MJD 5831.75–5857.86; Period 2 corresponds to MJD 5858.37–5892.97 and Period 3 corresponds to MJD 5901.42–5920.88.

for all measured pairs (a_i, b_j) with the pairwise lag $\Delta T_{ij} = t_j - t_i$. e_i and e_b , \bar{a} and \bar{b} , σ_a and σ_b are the measurement error, mean, standard deviation associated with the data set a_i and b_j respectively. DCF(τ) is obtained by averaging N number of pairs lying in the range $\tau - \frac{\Delta\tau}{2} < \Delta T_{ij} < \tau + \frac{\Delta\tau}{2}$ where $\Delta\tau=500s$.

$$DCF(\tau) = \frac{1}{N} UDCF_{ij}. \quad (9)$$

DCF evaluates the cross-correlation and possible time lags between the soft and hard energy band. The obtained DCF is fitted with the Gaussian function (Edelson & Krolik 1988) of the form:

$$DCF(\tau) = a \times \exp\left[\frac{-(\tau - \tau_{lag})^2}{(2\sigma^2)}\right], \quad (10)$$

where τ_{lag} is the time lag at which DCF peaks and σ is the width of Gaussian function (used in Gaur et al. 2015).

3.5. Power Spectral Density (PSD)

Power spectral density is the measure of variability power as a function of temporal frequency. It is used to characterize the temporal variations in flux and noise processes

in general. Periodogram is a tool to find hidden periodicities including any quasi-periodic oscillations (QPOs). It is defined as the modulus-squared of the Discrete Fourier Transform (DFT) of the data (Vaughan 2005). The obtained power spectrum consists of red noise which dominates over the measurement error i.e the poisson noise at the lower frequencies while the white noise dominates the red noise at higher frequencies which becomes equivalent to the poisson noise level of the data. The red noise part of the power spectrum is then fitted with a model of the form $P(f) = N f^{-m}$ where N is the normalisation and m is the power-law spectral index ($m > 0$) (van der Klis 1989; González-Martín & Vaughan 2012). Equations used in determining PSDs are provided in Appendix.

3.6. Spectral Analysis

The XSPEC software package version 12.11.1 is used for spectral fitting. The Galactic absorption n_H is fixed to be $1.0 \times 10^{21} \text{ cm}^{-2}$ (Lockman & Savage 1995) and the Xspec routine “cflux” is used to obtain unabsorbed flux and its error.

Massaro et al. (2004, 2008) found that blazars spectra are curved which arise due to log parabolic electron distributions. Therefore, they are well described by the log parabola model e.g., (Tramacere et al. 2007, 2009). We fit each spectra using models which are defined as follows:

TABLE 2
RESULTS OF DCF AND PSD ANALYSIS OF 1ES 1959+650.

Observation Date	τ_{lag} (ks)	σ (ks)	m	log(N)
2019-07-05	-0.94±0.10	7.53±0.12	-2.41±0.10	-10.13
2020-07-16	0.36±0.07	5.06±0.08	-2.15±0.03	-8.39

τ_{lag} & σ are the time lag at which DCF peaks & width of the Gaussian function fitting at DCF respectively;
m & N are slope & Normalization constant of the power law function fitting at PSD respectively.

1. Power law model, which is defined by $k E^{-\alpha}$. It is characterized by the photon index α , redshift z , and Normalization k .
2. The log-parabolic model *logpar*. It is characterized by photon index α , curvature β , and Normalization k .
3. Another form of log-parabolic model i.e. *eplogpar* model is used to calculate synchrotron peak E_p . Details of the equations are provided in Appendix.

4. RESULTS

We studied 125 archived observations of the Swift satellite of the TeV blazar 1ES 1959+650 during the period June 2018–December 2020. We also analyzed two publicly archived XMM–Newton observations of this blazar which are observed on 5th July 2019 and 16th July 2020. These observations are used to study flux and spectral variability of this blazar on intra-day as well as on long term timescales.

4.1. Intraday flux and spectral Variability

Blazar 1ES 1959+650 is studied with the XMM–Newton observations held on 5th July 2019 & 16th July 2020. The obtained light curves are shown in figure 1. Flux variability is calculated using excess variance and amplitude is calculated to be 1.95 and 3.12 % respectively. We also analyzed Swift–XRT observations of this source during the period June 2018–December 2020 in total 125 nights. The sample of light curves are shown in figure 2. We found significant flux variability (i.e $F_{var} > 3\sigma$) in five of these observations with amplitude varying between 4.11–7.34% which are presented in Table 1.

In order to calculate the spectral variability of these observations, HR analysis is performed which are presented in table 5. HR analysis yields no spectral variability for any individual light curve which can be seen from the plots of HR versus counts/s (0.3-10 keV) shown in figure 2.

4.2. Variability Timescale

Doubling/halving timescale τ_{var} defined in equation 7 is used to calculate the shortest variability timescales. The shortest variability timescale we found as $t_{var} = 15.28$ ks. Emission region size is constrained with the equation defined as follows:

$$R \leq \frac{\delta}{1+z} c \tau_{var} \quad (11)$$

with $\tau_{var}=15.27$ ks, Doppler factor $\delta=15$ (Patel et al. 2018) and it is found to be 6.56×10^{15} cm consistent

with values found in previous studies (MAGIC Collaboration et al. 2020; Shah et al. 2021).

4.3. Cross correlated variability and power spectral density

Cross correlation studies are performed using XMM–Newton data as they are long observations with high cadence. The cross-correlation between the soft band (0.3-2) keV and the hard band (2-10) keV is performed using DCF and their corresponding DCF plots are shown in the right panel of figure 1. The DCF plots are fitted with a Gaussian function (as described in section 3.4) and we have obtained a time lag of -0.94 and 0.36 ks respectively for the observations performed on 5th July 2019 and 16th July 2020 respectively. Results of DCF are provided in Table 2.

Significant correlation at positive/negative lags means that soft/hard variations are leading the variations in hard/soft bands respectively. During observation performed on 5th July 2019, the lags are negative i.e. the variations in the (2–10) keV are leading those in (0.3–2) keV. Therefore, in this case, variations at lower energies are slower than the variations at higher energies. The reverse situation is observed during the second observation. We found that there is a hard lag i.e. (2–10) keV band is lagging behind the soft one (0.3–2) keV. X-ray emission of HSPs lie at the top of the synchrotron hump and are characterised by the energy dependent acceleration and cooling mechanisms.

Following Zhang et al. (2002), the acceleration timescale t_{acc} and cooling timescale t_{cool} of the relativistic electrons in the observed frame can be expressed as a function of the observed photon energy E (in keV):

$$t_{acc}(E) = 9.65 \times 10^{-2} (1+z)^{3/2} \xi B^{-3/2} \delta^{-3/2} E^{1/2} \text{ s}, \quad (12)$$

$$t_{cool}(E) = 3.04 \times 10^3 (1+z)^{1/2} B^{-3/2} \delta^{-1/2} E^{-1/2} \text{ s}, \quad (13)$$

where z is the source's redshift, B is the magnetic field in Gauss, δ is the Doppler factor of the emitting region, and ξ is the parameter describing how fast the electrons can be accelerated.

One can note that t_{acc} and t_{cool} both depend on the photon energy in inverse fashion. The higher energy electrons cool faster as compared to lower energy electrons but accelerated slower than lower energy electrons. Therefore, if t_{cool} is greater than t_{acc} , cooling process dominates (Kirk et al. 1998). In such a case, higher energy photons will lead to lower energy photons and soft lag is expected.

$$\tau_{soft} = t_{cool}(E_l) - t_{cool}(E_h), \quad (14)$$

If t_{acc} is comparable to t_{cool} in the observed energy range, acceleration processes dominates in the emitting region and hard lag is expected. The time lag in an acceleration dominated system is expressed as:

$$\tau_{hard} = t_{acc}(E_h) - t_{acc}(E_l), \quad (15)$$

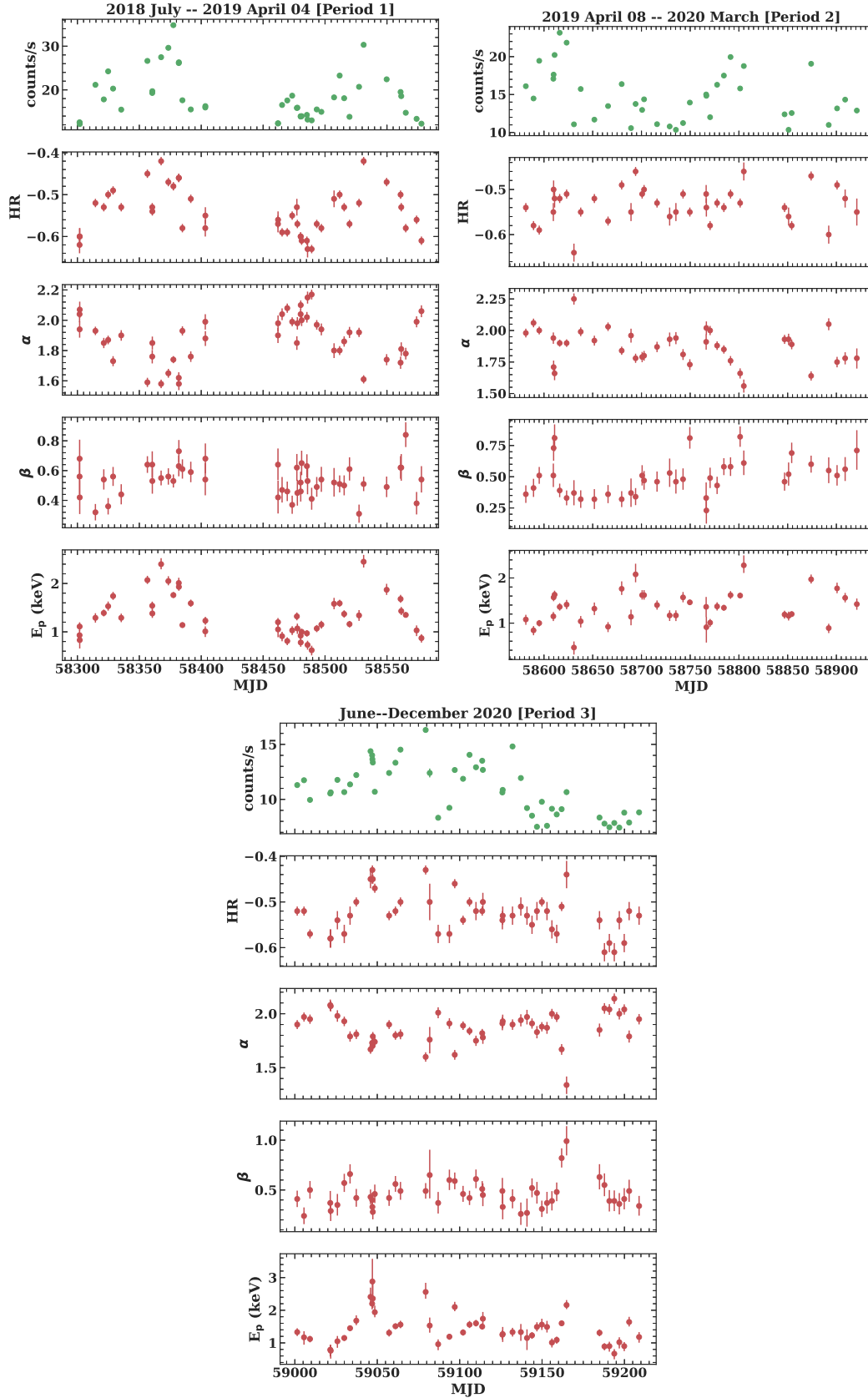


FIG. 4.— Temporal variations of various spectral parameters of blazar 1ES 1959+650 during different intervals. Best fit parameters are obtained with 2.7σ confidence interval.

TABLE 3
BEST SPECTRAL FIT PARAMETERS FOR THE POWER LAW AND LOG PARABOLIC MODEL OF BLAZAR 1ES 1959+650 OF XMM-NEWTON AND SWIFT-XRT OBSERVATIONS FROM JUNE 2018 TO DECEMBER 2020.

Observation ID	Fitting Model	α	β	$\log_{10}\text{Flux}$ (ergs/cm ² /s)	χ^2_{Red}	DoF	F-test	p-value	E_p (keV)	$L_p(10^{45})$ (erg/s)
XMM-Newton										
0850980101	PL	2.13 ^{+0.002} _{-0.002}	-	-9.16 ^{+0.001} _{-0.001}	41.47	175	-	-	-	-
	LP	2.06 ^{+0.002} _{-0.002}	0.22 ^{+0.005} _{-0.005}	-9.18 ^{+0.001} _{-0.001}	5.57	174	1129.34	5.37e-78	0.74(0.01)	1.20(0.002)
0870210101	PL	1.99 ^{+0.002} _{-0.002}	-	-9.27 ^{+0.001} _{-0.001}	29.67	175	-	-	-	-
	LP	1.89 ^{+0.003} _{-0.003}	0.24 ^{+0.006} _{-0.006}	-9.29 ^{+0.001} _{-0.001}	2.79	174	1687.02	1.83e-91	1.66(0.02)	0.89(0.002)
SWIFT-XRT										
00094153007	PL	2.2 ^{+0.021} _{-0.021}	-	-9.21 ^{+0.006} _{-0.006}	1.36	288	-	-	-	-
	LP	2.09 ^{+0.032} _{-0.033}	0.31 ^{+0.068} _{-0.067}	-9.24 ^{+0.009} _{-0.009}	1.14	287	56.59	6.93e-13	0.71(0.13)	1.12(0.02)
00094153008	PL	2.18 ^{+0.022} _{-0.022}	-	-9.25 ^{+0.006} _{-0.007}	1.15	280	-	-	-	-
	LP	2.06 ^{+0.034} _{-0.035}	0.36 ^{+0.073} _{-0.071}	-9.29 ^{+0.009} _{-0.009}	0.88	279	86.25	4.66e-18	0.83(0.12)	1.00(0.02)
00034588142	PL	2.21 ^{+0.022} _{-0.022}	-	-9.28 ^{+0.007} _{-0.007}	1.29	265	-	-	-	-
	LP	2.07 ^{+0.035} _{-0.036}	0.44 ^{+0.078} _{-0.075}	-9.32 ^{+0.010} _{-0.010}	0.90	264	116.88	8.55e-23	0.84(0.10)	0.96(0.02)
00034588143	PL	2.25 ^{+0.026} _{-0.025}	-	-9.31 ^{+0.007} _{-0.007}	1.07	241	-	-	-	-
	LP	2.15 ^{+0.037} _{-0.038}	0.32 ^{+0.085} _{-0.082}	-9.34 ^{+0.011} _{-0.011}	0.89	240	50.52	1.34e-11	0.58(0.15)	0.94(0.03)

PL: Power law; LP: Log Parabolic; DoF: Degree of Freedom; E_p : Peak Energy; L_p : Peak Luminosity.
Complete table of all observations appear in online supplementary material.

TABLE 4
SUMMARY OF SWIFT-XRT OBSERVATIONS OF 1ES 1959+650 DURING DIFFERENT PERIODS.

	Total Epoch	[MJD 58301.75–58577.86]	[MJD 58581.37–58920.97]	[MJD 59001.42–59208.88]
		Period 1	Period 2	Period 3
Mean counts/s	14.51	18.28	14.82	10.90
Maximum Flux (counts/s)	34.82	34.82	23.15	16.31
F_{var} (%)	33.97 (0.09)	29.96(0.14)	23.12(0.18)	21.43(0.20)
HR (max–min)	-0.42–-0.64	-0.42–-0.63	-0.46–-0.64	-0.43–-0.61
α (max–min)	2.25–1.34	2.17–1.58	2.25–1.56	2.14–1.34
β (max–min)	0.99–0.21	0.84–0.31	0.82–0.23	0.99–0.24
E_p (keV) (max–min)	2.88–0.46	2.45–0.62	2.28–0.46	2.88–0.67
Slope / intercept (E_p vs. L_p)	0.47(0.08) / -0.08(0.04)	0.85(0.08) / 0.06(0.04)	0.38(0.13) / -0.06(0.06)	0.45(0.08) / -0.41(0.04)
Slope / intercept (E_p vs. $1/\beta$)	-0.56(0.16) / 2.35(0.07)	-0.34(0.2) / 2.03(0.08)	-0.90(0.41) / 2.50(0.16)	-0.41(0.30) / 2.50(0.14)
Spearman's Correlation Coefficient				
	ρ_s (p-value)	ρ_s (p-value)	ρ_s (p-value)	ρ_s (p-value)
soft and hard counts/s	0.90 (7.13e-53)	0.97 (7.95e-28)	0.94 (1.79e-18)	0.95 (3.50e-24)
$Flux_{(0.3-10)keV}$ and HR	0.41 (5.53e-07)	0.86 (1.04e-14)	0.56 (2.98e-04)	0.64 (8.59e-07)
$Flux_{(0.3-10)keV}$ and α	-0.38(3.08e-06)	-0.73 (6.60e-09)	-0.40 (1.35e-02)	-0.52 (1.51e-04)
$Flux_{(0.3-10)keV}$ and E_p	0.39 (1.51e-06)	0.79 (5.30e-11)	0.44 (6.14e-03)	0.60 (6.10e-06)
α and β	-0.48 (2.00e-09)	-0.41 (4.18e-03)	-0.59 (1.05e-04)	-0.48 (6.38e-04)
E_p and α	-0.97 (1.73e-87)	-0.99 (6.74e-37)	-0.95 (3.22e-19)	-0.96 (2.15e-27)
E_p and $1/\beta$	-0.31 (2.04e-04)	-0.30 (3.84e-02)	-0.37 (2.36e-02)	-0.26 (7.09e-02)
E_p and L_p	0.35 (2.63e-05)	0.79 (3.08e-11)	0.41 (1.04e-02)	0.62 (2.45e-06)

max: maximum value; min: minimum value

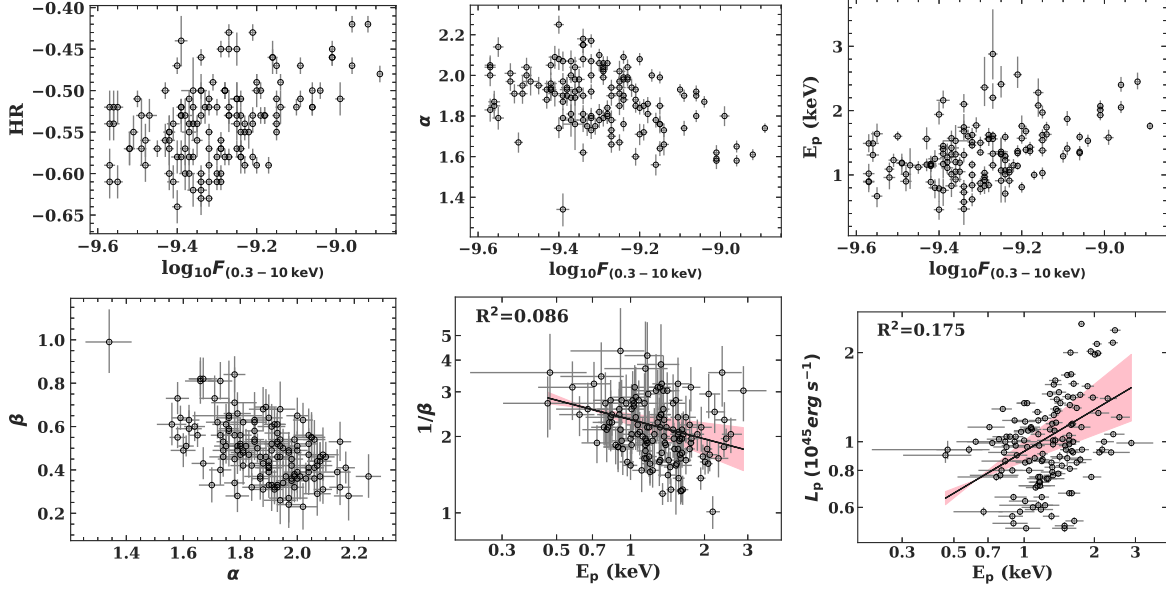


FIG. 5.— Correlation between various spectral parameters of blazar 1ES 1959+650.

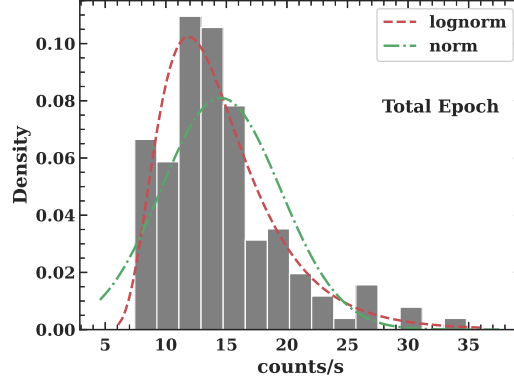


FIG. 6.— Fitting of Log-normal (red dashed line) and Normal (green dash-dotted line) distributions to count rate histogram of total epoch.

 TABLE 5
 RESULTS OF χ^2 TEST FOR HARDNESS RATIO ANALYSIS.

Obs. ID	Obs. Date	DoF	χ^2	$\chi^2_{0.90}$
XMM-Newton				
0850980101	2019-07-05	81	53.8	97.7
0870210101	2020-07-16	62	37.8	76.6
Swift-XRT				
00094153010	2018-07-02	16	3.4	23.5
00095332009	2019-06-17	33	12.4	43.7
00034588209	2020-06-21	21	7.0	29.6
00013906004	2020-12-10	30	5.1	40.2

#Complete table of all observations appear in online supplementary material

Using the observed lags, one can discern the physical parameters of the emitting region as follows:

$$B\delta\xi^{-2/3} = 0.21 \times (1+z) E_h^{1/3} \left[\frac{1 - (E_l/E_h)^{1/2}}{\tau_{\text{hard}}} \right]^{2/3} \text{ Gauss}, \quad (16)$$

$$B\delta^{1/3} = 209.91 \times \left(\frac{1+z}{E_l} \right)^{1/3} \left[\frac{1 - (E_l/E_h)^{1/2}}{\tau_{\text{soft}}} \right]^{2/3} \text{ Gauss}. \quad (17)$$

where τ_{hard} and τ_{soft} refer to the observed hard and soft lags (in second) between the low E_l and high E_h energy bands (in keV), respectively, (E_l and E_h are logarithmic averaged energies of the given energy bands).

Equation 17 is used to calculate the magnetic field with redshift $z=0.048$, $\tau_{\text{soft}}=940$ sec and Doppler factor $\delta=15$ (Patel et al. 2018). Magnetic field, B of the emitting region is found to be 0.64 ± 0.05 Gauss which is found to be consistent with the values provided in the literature. Tagliaferri et al. (2003) and MAGIC Collaboration et al. (2020) performed SED modeling and obtained magnetic field close to the value we have obtained.

4.4. Long Term flux and spectral Variability

We study long term flux and spectral variability of blazar 1ES 1959+650, observed between the period June 2018–December 2020. Depending on the flux state of the blazar, we have divided the total epoch into three periods. The flux state of the source is defined with respect

to the average counts during our observing run. The source is in high state during period 1 [MJD 58301.75–58577.86] which is during 2018 July–2019 April 04), in an intermediate state during period 2 [MJD 58581.37–58920.97] which is 2019 April 08–2020 March and in low flux state during period 3 [MJD 59001.42–59208.88] which is June–December 2020 with the mean count rate of 18.28, 14.82 and 10.90 counts/s respectively. The long term light curve of the blazar 1ES 1959+650, observed during the period June 2018–December 2020, is shown in figure 3. The light curves for different periods are shown in figure 4. During long term timescales, the source showed significant spectral variability. The HR, α , β and E_p have showed long term variations which can be seen in figure 4 for different periods.

In period 1, source exhibit two flares with flux reaches upto $128.82 \times 10^{-11} \text{ erg cm}^{-2} \text{ s}^{-1}$ on 2018-09-16. Fractional variability amplitude F_{var} is found to be $\sim 29.96\%$ and significant spectral variability is also found during this period. Photon index has hardened with increase in flux of the source which varies between 2.17–1.58. Lower values of curvature parameter are found which ranges between 0.84–0.31. Peak energy shows positive correlation with respect to flux of the source and reached upto 2.45 keV. During Period 2, source exhibits small flares with mean flux level of this period reaching upto $52.93 \times 10^{-11} \text{ erg cm}^{-2} \text{ s}^{-1}$. F_{var} is found to be 23.12% and significant spectral variability is also found during this period which can be seen in Fig 4. Photon index has hardened with increase in flux of the source which varies between 2.25–1.56. Similar to Period 1, β has lower values which ranges between 0.82–0.23. During Period 3, source exhibit relatively low flux state with highest flux reaching upto $61.66 \times 10^{-11} \text{ erg cm}^{-2} \text{ s}^{-1}$. F_{var} is found to be 21.43% and significant spectral variability is found during this period. Photon index has hardened with increase in flux of the source which varies between 2.14–1.34. β has lower values ranging between 0.99–0.24. E_p is positively correlated with flux and reaches upto 2.88 keV.

4.5. Log Normality of flux distributions

The nature of variability in a long term period can be quantified or explained with the flux distribution of the variable source (Uttley et al. 2005). Blazars exhibits a log-normal flux distribution over the normal distribution (Uttley et al. 2005; Chakraborty 2020; Shah et al. 2020) which could be an indication of the variability imprint of the accretion disk onto the jet. The flux distribution is expected to be a Gaussian for a linear stochastic process, while it is expected to be a lognormal for multiplicative processes that originate in the accretion disk (Uttley et al. 2005). The fluctuations of the log-normal fluxes are proportional to the flux itself and indicates underlying multiplicative physical processes. The lognormality of blazars on different time scales and in different spectral ranges are studied many times in literature (i.e. Kushwaha et al. 2016; Sinha et al. 2017; Chevalier et al. 2019; Bhatta & Dhital 2020). However, the dominance of doppler boosted jet emission in blazars

restricts our understanding of the accretion disc-jet connection. Kushwaha et al. (2016) performed an extensive study of lognormality of flux distribution of blazars for the first time. Specifically, variations on minutes/hours like timescales should be independent of accretion disc perturbations and favours originating from the instabilities in the relativistic jets (Gaidos et al. 1996; Albert et al. 2007; Narayan & Piran 2012). As blazars have strong magnetized jets pointing towards us, flux distributions using minijet-in-a-jet model (Giannios et al. 2009) are studied by Biteau & Giebels (2012) and they found that the flux from a single randomly oriented mini jet will follow a Pareto distribution. The flux integrated from many isotropically oriented mini jets could lead to an α stable distribution which could converge to a log normal distribution when subjected to experimental uncertainties. Therefore, non-linear flux distributions can arise from small Gaussian perturbations. This could provide an explanation for the lognormal flux distributions in blazars during flaring states. In this scenario, flux distribution has been found to hold the rms-flux relation (Biteau & Giebels 2012).

An alternative interpretation for the non-Gaussian distribution of blazar variability light curves is provided by Sinha et al. (2018). They explained it using a small perturbation in the acceleration timescale which can result in the variability of the particle number density that is a linear combination of Gaussian and lognormal processes. The dominant shape of the resultant flux distribution is determined by relative weight of these processes (Sinha et al. 2018; Bhatta & Dhital 2020). They also demonstrated that perturbation in the acceleration time-scale leads to Gaussian distribution in its photon index, whereas perturbation in the particle cooling rate produces neither of these distributions (Sinha et al. 2018; Shah et al. 2018, 2020; Khatoun et al. 2020, 2022, and references therein).

Flux distribution of 1ES 1959+650 is studied by Patel et al. (2018) using radio to γ -ray data. It is also studied by Bhatta & Dhital (2020) using decade-long Fermi/LAT observations. Duda & Bhatta (2021) used maximum likelihood estimation (MLE) methods to study flux distributions.

In order to investigate log normality of flux distribution in our observations, we fit the histograms of the X-ray data observed by Swift-XRT between the period June 2018 to December 2020 with the Gaussian and log-normal distributions. The figure 6 shows the log-normal and normal flux distribution of this blazar for the total epoch used in this analysis. We have used Anderson-Darling (AD) test (e.g. Anderson & Darling 1952, 1954; Jäntschi & Bolboacă 2018; Stephens 1977; D’Agostino 1986; Shah et al. 2018) to quantify the nature of flux distribution of blazar 1ES 1959+650. We have obtained that the blazar 1ES 1959+650 follows a log-normal behaviour in total epoch with a p -value = 0.20. We also found a significant linear correlation between rms and flux for the total epoch which indicates that the variability might arise from the minijet-in-a-jet model. However, as recently shown by Scargle (2020), the linear rms-flux relationship can be obtained from intrinsically additive processes, therefore this result might be used with cau-

tion. We also calculated the photon index distribution for the total epoch and found it to be well fitted with log-normal as well as normal distributions. As discussed in Sinha et al. (2018), small temporal fluctuations in the intrinsic time-scales in the acceleration region is capable of producing particle distributions with non-Gaussian signatures and significant flux-rms correlations. Therefore, we cannot rule out the possibility of an acceleration-due-to-shock scenario.

4.6. Relation between spectral parameters

Blazar 1ES 1959+650 spectra are fit by log parabolic and power law models. The results of both the models are presented in table 3. We used the F-test to compare the fitting results of these two models. We found that all the spectra are well fitted by a log parabolic model. Then, we derived the spectral fitting parameters i.e. location of synchrotron peak (E_p), peak luminosity (L_p) with the log parabolic model. The results show the variation in E_p in the range of 0.46–2.88 keV whereas L_p varies in the range of 0.51–2.50 erg cm⁻² s⁻¹. Spectral variations of the photon index varies between 1.34–2.25 and the curvature (β) varies between 0.21–0.99. Correlation between various spectral parameters are shown in figure 5 and are studied with Spearman’s rank correlation coefficient ρ_s and their corresponding p -values. The results are presented in table 4.

A positive correlation is expected between photon index α and curvature β in the first order fermi acceleration scenario. This correlation is predicted for the energy dependent acceleration probability process EDAP (i.e. Massaro et al. 2004) where the probability p_i that a particle undergoes an acceleration step i , with the corresponding energy γ_i^q and energy gain ε , is given by $p_i = g/\gamma_i^q$ where g and q are positive constants. Therefore, as the energy of the particle increases, the probability of the particle’s acceleration decreases. According to Massaro et al. (2004), a linear relationship is expected between spectral index s and curvature r , $s = -r(2/q) \log g/\gamma_0 - (q-2)/2$. The synchrotron emission is produced by the differential energy spectrum of the form $N(\gamma) \sim \gamma/\gamma_0^{-s-r \log \gamma/\gamma_0}$ is given by $P_S(\nu) \propto (\nu/\nu_0)^{-(a+b \log(\nu/\nu_0))}$ with $a = (s-1)/2$ and $b = r/4$ (i.e. Massaro et al. 2004). In our observations, we found weak negative correlation between α and β which is expected when $g > \gamma_0$ (i.e. Kapanadze et al. 2020). It implies that there exists electron population with a very low initial energy γ_0 in the emission zone. Kapanadze et al. (2020) found a negative correlation between these quantities for Mrk 421 for some of its observational period during 2015 December–2018 April. The co-existence of second order Fermi acceleration/stochastic acceleration could also weaken the α – β correlation. Katarzyński et al. (2006) have shown via simulations that electrons can be accelerated at the shock front via EDAP but can gain energy via the stochastic mechanism after escaping the shock front. The combined effect of both such processes could result in a weak or no strong correlation between α and β . (Kapanadze et al. 2016b; Kapanadze 2018; Kapanadze et al. 2020).

The synchrotron peak energy (E_p) and the luminosity (L_p) of a source follows a power-law relation of the form $L_p \propto E_p^a$ (i.e. Rybicki & Lightman 1979). If the elec-

tron distribution in the emitting region follows a log-parabolic distribution, the peak luminosity is given by $L_p \sim N\gamma_p^2 B^2 \delta^4$. The peak energy follows $E_p \sim \gamma_p^2 B \delta$ (e.g., Tramacere et al. 2009). γ_p represents the peak of $n(\gamma)\gamma$ where γ is the electron Lorentz factor; $N \sim n(\gamma_p)\gamma_p$ is the total electron number, B represents the magnetic field and δ is the Doppler beaming factor. If $a = 1$, the spectral changes are mainly caused by the variations of the average electron energy, but the total electron number remains constant; if $a = 1.5$, they are mainly caused by the variations of the average electron energy, but the total electron number also changes; if $a = 2$, they are correlated with the changes of magnetic field, B ; and if $a = 4$, they might be dominated by the variations of the beaming factor, δ . We found significant correlations between E_p and L_p during our observations. We fit our observational data using the equation $\log L_p = a \log E_p + b$ and found a to be < 1 during the whole observational period. During period 1, $a \sim 1$ which concludes that the spectral changes might be caused by the variations of the average electron energy.

The correlation between E_p and β provides us clues about the acceleration mechanism (e.g. Massaro et al. 2004; Tramacere et al. 2011) whether it is statistical/stochastic mechanisms. These two mechanisms are produced by the log-parabolic electron distribution, resulting in a log-parabolic SED.

In statistical acceleration process, the electron energy distribution follows the log-parabolic law and the acceleration efficiency of the emitting electrons is inversely proportional to their energy (Massaro et al. 2004). Therefore, in such process, E_p and β follow the correlation of the form $\log E_p \approx Const. + 2/(5\beta)$, with the assumption of $\beta = r/4$ where r is the curvature of the electron energy distribution (Chen 2014). For the fluctuations of fractional acceleration gain process, electron energies follow log-normal law, and the energy gain fluctuations are a random variable around the systematic energy gain (Tramacere et al. 2011). In such case, E_p and β follow the correlation of $\log E_p \approx Const. + 3/(10\beta)$ given $\beta = r/4$ (Chen 2014).

Second scenario is described by the stochastic acceleration process. Here, a momentum-diffusion term is included in the kinetic equation, which leads to energy gain fluctuations in the diffusive shock acceleration process (Tramacere et al. 2011). In this process, E_p and β follows the relation of $\log E_p \approx Const. + 1/(2\beta)$ where $\beta = r/4$ (Chen 2014). Therefore, theoretically expected values of C are 10/3, 5/2 and 2 for the fractional acceleration gain fluctuation, energy-dependent acceleration probability and stochastic acceleration processes, respectively. We found a significant negative correlation between E_p and $1/\beta$ in our observations. We fit our observational data using the equation $1/\beta = C \log E_p + D$ but did not get the value of C close to the above values hence we cannot explain our observational data using any of the above acceleration mechanism. However, the co-existence of the above acceleration mechanism might be possible (Wang et al. 2019) which could lead to overall weakening of correlation.

A positive correlation between flux and E_p is found dur-

ing our observations which indicates the shift of synchrotron peak to higher energies. Also, we found significant correlation between flux and S_p which is expected as peak height increases as flux increases (Holder et al. 2003; Kapanadze et al. 2016b,a, 2018a,b; Wang et al. 2019; Chandra et al. 2021). Near the peak energy of the emission, the cooling timescale shortens and can complete with the acceleration timescales (Tramacere et al. 2009) which leads to an anti-correlation between E_p and β if the cooling timescales is shorter than that of EDAP or stochastic acceleration.

We found significant correlation between flux and α which is an indication of hardening of the spectra as flux increases which is very common for HSP type blazars. It indicates that the hard X-rays are varying more rapidly than soft X-rays (Cui 2004; Giebels et al. 2002; Tagliaferrri et al. 2003; Holder et al. 2003) or there is an injection of fresh electrons with an energy distribution harder than the previously cooled electrons (Mastichiadis & Kirk 2002).

5. DISCUSSION

We observed the blazar 1ES 1959+650 during the period June 2018–December 2020 when the source showed different flux states (high/low) to study their flux and spectral variability on intra-day and long term timescales using SWIFT satellite. The source is studied for intra-day flux variability in total 125 nights and found significant variability in only five nights. We did not find any spectral variability during these observations. The source is studied using two observations of XMM–Newton held on 5th July 2019 and 16th July 2020 and found significant flux variability in both of these observations with low amplitude variation of 1.95% and 3.12% respectively. The source is favoured by the shock-in-jet model where IDV is triggered by the interaction of the shock front with jet inhomogeneities; turbulence behind a shock front; smallest-size jet turbulent structures (i.e. Marscher & Gear 1985; Wagner & Witzel 1995; Sokolov et al. 2004). Smallest size jet structures are attributed to produce very rapidly variable emission due to light travel arguments. We found flux doubling timescale of 15.27 ks (between MJD 58670.07–58670.13) which leads to size of the emitting region to be 6.56×10^{15} cm and black hole mass estimate of $2.95 \times 10^8 M_\odot$ which is obtained as follows:

$$M_{BH} = \frac{c^3 t_{var}}{10G(1+z)} \quad (18)$$

where G is the Gravitational constant (e.g. Zhang et al. 2021)). Yuan et al. (2015) reported the optical timescales in the range from 23 minutes to 3.72 hr with the Kerr black hole mass in the range $(0.42-4.09) \times 10^8 M_\odot$. Falomo et al. (2003) used the host galaxy luminosity relation and Kurtanidze et al. (2009) used the variability timescales to estimate the black hole mass to be $3.16 \times 10^8 M_\odot$.

XMM–Newton observation of 1ES 1959+650 during two observations suggest the presence of soft as well as hard lags which infers that t_{acc} and t_{cool} of the emitting region changes from epoch to epoch. This is consistent with previous studies. Hard lags suggest that the flux evolution is dominated by acceleration processes while soft lags sug-

gest that the emission region is dominated by cooling mechanisms. The first-order Fermi acceleration process (e.g. Kirk et al. 1998, and references therein) and statistical/stochastic processes involving second-order Fermi acceleration (Katarzyński et al. 2006; Becker et al. 2006) are most acceptable models for particle acceleration and therefore, hard delays are modulated by variations of the acceleration parameter ξ . We have estimated the value of magnetic field to be 0.64 ± 0.05 Gauss using the soft lags and the values are found to be close to those reported in literature for our source.

PSD analysis is done using two observations of XMM–Newton which are used to characterize the variability on intra-day timescales. Accretion disc models typically produce PSD slopes in the range between $-1.30 - -2.10$ (Zhang & Bao 1991; Mangalam & Wiita 1993; Kelly et al. 2011) while jet based models yield steeper slopes in the range between $-1.70 - -2.90$ (i.e. Calafut & Wiita 2015; Pollack et al. 2016; Wehrle et al. 2019). The observed PSD slopes of -2.41 and -2.15 for intra-day light curves are steeper as compared to those predicted by accretion disk models and are more consistent with jet based models. However, the small number of PSDs used here provides a tentative hint favouring fluctuations originating in jets.

On long term timescales, source exhibit high state during Period 1 with two flares with flux reaching upto 34.82 counts/s. During Period 2, the flux of the source decreases to 10.35 counts/s and during Period 3, the flux of the source is lowest with reaching upto 7.43 counts/s. Source showed significant spectral variability throughout our observations. We studied flux distributions of our source during different observational periods and found that the source follows a log-normal behaviour during the total epoch. Kapanadze et al. (2020) studied the log-normality of Mrk 421 using the multi-wavelength data and found that log-normal fits were preferred over normal fits for most of their dataset. The flux variability of the source is attributed to the propagation of shocks downstream the relativistic jets (Sokolov et al. 2004). The formation of these shocks might be related to the turbulence/inhomogeneities occurring in the accretion disk (Kushwaha et al. 2016; Sinha et al. 2017; Kapanadze et al. 2020; Kushwaha & Pal 2020). However, this is not always the case. Many observations including flaring events showed deviations from log-normal distribution which indicates that these flares might be triggered by the interaction of shocks with the jet inhomogeneities which could be related to the jet instabilities (i.e. Marscher 2014).

All the spectra are well described by log parabolic model yielding spectral curvature ranging between $0.23-0.99$ and photon index varies between $1.34-2.25$. During our observations, peak energy E_p varies in such a way that E_p shifts upto higher energies as flux increases. We studied correlation between the spectral parameters derived from log parabolic model. We found weak negative correlation between α and β which is due to the co-existence of stochastic and statistical acceleration processes (Kapanadze et al. 2018b; Kapanadze 2018). The spectral hysteresis analysis of 1ES 1959+650 showed an interplay between the acceleration and cool-

ing timescales of emitting particles and flux variability timescale (Kapanadze et al. 2018a,b). Correlation between E_p and L_p also follows a powerlaw as described in section 4.6. During Period 1, we found spectral changes to be caused by the variations of the average electron energy. The anti-correlation between E_p and β is expected for the efficient stochastic acceleration of electrons by the magnetic turbulence which is not seen in our observations. The weak correlation between these parameters implies the co-existence of stochastic and statistical acceleration processes in the emitting region.

6. CONCLUSION

The main findings of this work are summarized as follows:

1. Swift-XRT and XMM–Newton EPIC-pn observations have been used to study the HSP 1ES 1959+650 during the period June 2018–December 2020 in total 127 nights of observations. Significant variability is detected in total 7 of the nights with flux variability amplitude varying between 1.95–3.12 %. Hardness ratio analysis shows no significant spectral variability in any of the nights. The flux doubling timescale is found to be 15.27 ks and the black hole mass is calculated to be $2.95 \times 10^8 M_\odot$.
2. Using XMM–Newton observations, cross-correlation between soft band (0.3–2) keV and hard band (2–10) keV were performed using the DCF method. Both DCF plots are correlated and hard as well as soft lag of 360 and 940 seconds respectively are found which provides magnetic field strength of $\sim 0.64 \pm 0.05$ Gauss in the jet.
3. PSD analysis is performed using XMM–Newton observations and power law slopes are found to be -2.41 and -2.15 which favours jet based model (as discussed in section 5).
4. Intra-day light curves are checked for lognormality behaviour and found that they are well modelled by normal as well as lognormal distributions. As suggested by Gaidos et al. (1996); Narayan & Piran (2012), variations on minutes/hours like timescales are independent of accretion disc fluctuations and could be attributed to some linear/non-linear perturbations in the physical parameters used to model the relativistic jets in blazars. The most plausible model to explain short-term variability is turbulence in the jet behind the re-confinement shock that contains multiple synchrotron emitting cells of different sizes within the single emitting region which yields impressive light curves, PSDs and polarization variations (i.e. Pol-

lack et al. 2016; Marscher 2014).

5. Source exhibits log normality behaviour on long term timescales. Long term variations are explained by superposition of small flares on long term trends. As blazar jets are highly magnetized, variability may be incorporated by minijets-in-a-jet model as we found a linear correlation between rms–flux relation. However, as the photon index distribution is well fitted by Gaussian as well as normal distributions, we can not rule out the possibility of propagation and evolution of relativistic shocks through the jet leading to variability in X-ray bands. These shocks could be related to an abrupt increase of the plasma injection rate at the jet base owing to the instabilities in the accretion disc.
6. On the long timescales, source showed high as well as low flux states. Log parabolic model is required to describe the X-ray spectra of this source yielding spectral curvature values ranges between 0.23–0.99 and photon index ranges between 1.34–2.25. Position of synchrotron SED peak E_p varies between 0.46–2.88 keV. Synchrotron peak E_p strongly correlates with flux which implies that E_p increases as flux increases. Hardness ratio analysis on long term timescales indicates that the source follows the ‘harder-when-brighter’ trend.
7. Source showed weak correlation between photon index α and curvature β which could be due to the combined effect of statistical/stochastic processes. Electrons can be accelerated at the shock front via EDAP but they can gain energy via the stochastic mechanism after escaping the shock front (Katarzyński et al. 2006).
8. 1ES 1959+650 showed a low spectral curvature ($\beta \sim 0.23$ –0.99) and an anti-correlation between E_p versus $1/\beta$ is found which might be due to the co-existence of stochastic and statistical acceleration processes.

ACKNOWLEDGEMENTS

We would like to thank the anonymous reviewer for the constructive comments that helped us to improve the paper scientifically. We acknowledge the use of public data from the Swift data archive. This research is based on observations obtained with XMM-Newton, an ESA science mission with instruments and contributions directly funded by ESA Member States and NASA. KAW and HG acknowledge the financial support from the Department of Science and Technology, India through INSPIRE Faculty award IFA17-PH197 at ARIES, Nainital.

APPENDIX

For an evenly sampled light curve (with a sampling period ΔT) comprising a series of fluxes x_i measured at discrete times t_i ($i = 1, 2, \dots, N$):

$$|DFT(f_j)|^2 = \left| \sum_i x_i e^{2\pi i f_j t_i} \right|^2, \quad (1)$$

at $N/2$ evenly spaced frequencies $f_j = \frac{j}{N\Delta T}$ (where $j = 1, 2, \dots, N/2$), $f_{N/2} = \frac{1}{2\Delta T}$ is the Nyquist frequency, f_{Nyq} which denotes the maximal frequency that can be meaningfully inferred.

To eliminate the zero frequency power it is important to subtract the mean flux from the light curve before calculating the DFT (Vaughan et al. 2003b).

PSD is then defined as (Vaughan 2005):

$$P(f_j) = \frac{2\Delta T}{N\bar{x}^2} |DFT(f_j)|^2. \quad (2)$$

The log-parabolic model is given by

$$F(E) = K(E/E_1)^{(-\alpha - \beta \log(E/E_1))}, \quad (3)$$

in units of photons $\text{cm}^{-2} \text{s}^{-1} \text{keV}^{-1}$ (e.g., Massaro et al. 2004). E_1 is the reference energy, generally fixed to 1 keV. The parameter α is the spectral index at the energy of E_1 , while β is the curvature parameter around the peak. K is the normalization constant. The location of the synchrotron peak is calculated by

$$E_{p, \logpar} = E_1 10^{(2-\alpha)/2\beta} (\text{keV}), \quad (4)$$

Another form of log-parabolic model i.e. *eplogpar* model is used to calculate synchrotron peak E_p . It is defined as

$$F(E) = K 10^{-\beta(\log(E/E_p))^2} / E^2, \quad (5)$$

in units of photons $\text{cm}^{-2} \text{s}^{-1} \text{keV}^{-1}$. (e.g. Tramacere et al. 2007, 2009). E_p is the synchrotron peak in units of keV, β is the curvature parameter, which is the same as the parameter β in the above log-parabolic model. The parameter K is the flux in νF_ν units at energy E_p keV.

REFERENCES

- Abdo, A. A., Ackermann, M., Agudo, I., et al. 2010, ApJ, 716, 30, doi: 10.1088/0004-637X/716/1/30
- Albert, J., Aliu, E., Anderhub, H., et al. 2007, ApJ, 669, 862, doi: 10.1086/521382
- Anderson, T. W., & Darling, D. A. 1952, The Annals of Mathematical Statistics, 23, 193, doi: 10.1214/aoms/1177729437
- . 1954, Journal of the American Statistical Association, 49, 765, doi: 10.1080/01621459.1954.10501232
- Becker, P. A., Le, T., & Dermer, C. D. 2006, ApJ, 647, 539, doi: 10.1086/505319
- Beckmann, V., Wolter, A., Celotti, A., et al. 2002, A&A, 383, 410, doi: 10.1051/0004-6361/20011752
- Bhatta, G., & Dhital, N. 2020, ApJ, 891, 120, doi: 10.3847/1538-4357/ab7455
- Biteau, J., & Giebels, B. 2012, A&A, 548, A123, doi: 10.1051/0004-6361/201220056
- Blandford, R. D., & Rees, M. J. 1978, Phys. Scr, 17, 265, doi: 10.1088/0031-8949/17/3/020
- Böttcher, M., Reimer, A., Sweeney, K., & Prakash, A. 2013, ApJ, 768, 54, doi: 10.1088/0004-637X/768/1/54
- Burrows, D. N., Hill, J. E., Nousek, J. A., et al. 2005, Space Sci. Rev., 120, 165, doi: 10.1007/s11214-005-5097-2
- Calafut, V., & Wiita, P. J. 2015, Journal of Astrophysics and Astronomy, 36, 255, doi: 10.1007/s12036-015-9324-2
- Chakraborty, N. 2020, Galaxies, 8, 7, doi: 10.3390/galaxies8010007
- Chandra, S., Boettcher, M., Goswami, P., et al. 2021, ApJ, 918, 67, doi: 10.3847/1538-4357/ac01d1
- Chen, L. 2014, ApJ, 788, 179, doi: 10.1088/0004-637X/788/2/179
- Chevalier, J., Sanchez, D. A., Serpico, P. D., Lenain, J. P., & Maurin, G. 2019, MNRAS, 484, 749, doi: 10.1093/mnras/stz027
- Cui, W. 2004, ApJ, 605, 662, doi: 10.1086/382587
- Dermer, C. D., Schlickeiser, R., & Mastichiadis, A. 1992, A&A, 256, L27
- Dhiman, V., Gupta, A. C., Gaur, H., & Wiita, P. J. 2021, MNRAS, 506, 1198, doi: 10.1093/mnras/stab1743
- Duda, J., & Bhatta, G. 2021, MNRAS, 508, 1446, doi: 10.1093/mnras/stab2574
- D'Agostino, R.B.; Stephens, M. 1986, Marcel-Dekker: New York, NY, USA, 123, 146
- Edelson, R., Turner, T. J., Pounds, K., et al. 2002, ApJ, 568, 610, doi: 10.1086/323779
- Edelson, R. A., & Krolik, J. H. 1988, ApJ, 333, 646, doi: 10.1086/166773
- Edelson, R. A., Krolik, J. H., & Pike, G. F. 1990, ApJ, 359, 86, doi: 10.1086/169036
- Elvis, M., Plummer, D., Schachter, J., & Fabbiano, G. 1992, ApJS, 80, 257, doi: 10.1086/191665
- Falomo, R., Carangelo, N., & Treves, A. 2003, MNRAS, 343, 505, doi: 10.1046/j.1365-8711.2003.06690.x
- Foschini, L., Ghisellini, G., Tavecchio, F., Bonoli, G., & Stamerra, A. 2011, A&A, 530, A77, doi: 10.1051/0004-6361/201117064
- Fromm, C. M., Ros, E., Perucho, M., et al. 2013, A&A, 557, A105, doi: 10.1051/0004-6361/201321784
- Gaidos, J. A., Akerlof, C. W., Biller, S., et al. 1996, Nature, 383, 319, doi: 10.1038/383319a0
- Gaur, H., Mohan, P., Wierzczołska, A., & Gu, M. 2018, MNRAS, 473, 3638, doi: 10.1093/mnras/stx2553
- Gaur, H., Gupta, A. C., Bachev, R., et al. 2015, A&A, 582, A103, doi: 10.1051/0004-6361/201526536
- Gehrels, N., Chincarini, G., Giommi, P., et al. 2004, ApJ, 611, 1005, doi: 10.1086/422091
- Ghisellini, G., Celotti, A., Fossati, G., Maraschi, L., & Comastri, A. 1998, MNRAS, 301, 451, doi: 10.1046/j.1365-8711.1998.02032.x
- Ghisellini, G., & Maraschi, L. 1989, ApJ, 340, 181, doi: 10.1086/167383
- Ghosal, B., Tolamatti, A., Bhattacharyya, S., et al. 2022, MNRAS, 517, 5473, doi: 10.1093/mnras/stac2950
- Giannios, D., Uzdensky, D. A., & Begelman, M. C. 2009, MNRAS, 395, L29, doi: 10.1111/j.1745-3933.2009.00635.x
- Giebels, B., Bloom, E. D., Focke, W., et al. 2002, ApJ, 571, 763, doi: 10.1086/340065
- González-Martín, O., & Vaughan, S. 2012, A&A, 544, A80, doi: 10.1051/0004-6361/201219008
- Holder, J., Bond, I. H., Boyle, P. J., et al. 2003, ApJ, 583, L9, doi: 10.1086/367816

- Jansen, F., Lumb, D., Altieri, B., et al. 2001, *A&A*, 365, L1, doi: 10.1051/0004-6361:20000036
- Jäntschi, L., & Bolboacă, S. D. 2018, *Mathematics*, 6, doi: 10.3390/math6060088
- Kapanadze, B. 2018, *Galaxies*, 6, 125, doi: 10.3390/galaxies6040125
- Kapanadze, B., Dorner, D., Romano, P., et al. 2017, *ApJ*, 848, 103, doi: 10.3847/1538-4357/aa8ea6
- Kapanadze, B., Dorner, D., Vercellone, S., et al. 2016a, *MNRAS*, 461, L26, doi: 10.1093/mnrasl/slw054
- Kapanadze, B., Romano, P., Vercellone, S., et al. 2016b, *MNRAS*, 457, 704, doi: 10.1093/mnras/stv3004
- Kapanadze, B., Vercellone, S., & Romano, P. 2020, *New Astronomy*, 79, 101393, doi: <https://doi.org/10.1016/j.newast.2020.101393>
- Kapanadze, B., Dorner, D., Vercellone, S., et al. 2018a, *MNRAS*, 473, 2542, doi: 10.1093/mnras/stx2492
- . 2018b, *ApJS*, 238, 13, doi: 10.3847/1538-4365/aad8b5
- Kapanadze, B., Gurchumelia, A., Dorner, D., et al. 2020, *ApJS*, 247, 27, doi: 10.3847/1538-4365/ab6322
- Katarzyński, K., Ghisellini, G., Tavecchio, F., Gracia, J., & Maraschi, L. 2006, *MNRAS*, 368, L52, doi: 10.1111/j.1745-3933.2006.00156.x
- Kaur, N., Chandra, S., Baliyan, K. S., Sameer, & Ganesh, S. 2017, *ApJ*, 846, 158, doi: 10.3847/1538-4357/aa86b0
- Kelly, B. C., Sobolewska, M., & Siemiginowska, A. 2011, *ApJ*, 730, 52, doi: 10.1088/0004-637X/730/1/52
- Khatoun, R., Prince, R., Shah, Z., Sahayanathan, S., & Gogoi, R. 2022, *MNRAS*, 513, 611, doi: 10.1093/mnras/stac892
- Khatoun, R., Shah, Z., Misra, R., & Gogoi, R. 2020, *MNRAS*, 491, 1934, doi: 10.1093/mnras/stz3108
- Kirk, J. G., Rieger, F. M., & Mastichiadis, A. 1998, *A&A*, 333, 452, doi: 10.48550/arXiv.astro-ph/9801265
- Krawczynski, H., Hughes, S. B., Horan, D., et al. 2004, *ApJ*, 601, 151, doi: 10.1086/380393
- Kurtanidze, O. M., Tetradze, S. D., Richter, G. M., et al. 2009, in *Astronomical Society of the Pacific Conference Series*, Vol. 408, *The Starburst-AGN Connection*, ed. W. Wang, Z. Yang, Z. Luo, & Z. Chen, 266
- Kushwaha, P., Chandra, S., Misra, R., et al. 2016, *ApJ*, 822, L13, doi: 10.3847/2041-8205/822/1/L13
- Kushwaha, P., & Pal, M. 2020, *Galaxies*, 8, 66, doi: 10.3390/galaxies8030066
- Landau, R., Golisch, B., Jones, T. J., et al. 1986, *ApJ*, 308, 78, doi: 10.1086/164480
- Larionov, V. M., Jorstad, S. G., Marscher, A. P., et al. 2020, *MNRAS*, 492, 3829, doi: 10.1093/mnras/staa082
- Lockman, F. J., & Savage, B. D. 1995, *ApJS*, 97, 1, doi: 10.1086/192133
- MAGIC Collaboration, Acciari, V. A., Ansoldi, S., et al. 2020, *A&A*, 638, A14, doi: 10.1051/0004-6361/201935450
- Mangalam, A. V., & Wiita, P. J. 1993, *ApJ*, 406, 420, doi: 10.1086/172453
- Mannheim, K., & Biermann, P. L. 1992, *A&A*, 253, L21
- Marscher, A. P. 2014, *ApJ*, 780, 87, doi: 10.1088/0004-637X/780/1/87
- Marscher, A. P., & Gear, W. K. 1985, *ApJ*, 298, 114, doi: 10.1086/163592
- Marscher, A. P., Jorstad, S. G., D’Arcangelo, F. D., et al. 2008, *Nature*, 452, 966, doi: 10.1038/nature06895
- Massaro, E., Perri, M., Giommi, P., & Nesci, R. 2004, *A&A*, 413, 489, doi: 10.1051/0004-6361:20031558
- Massaro, F., Tramacere, A., Cavaliere, A., Perri, M., & Giommi, P. 2008, *A&A*, 478, 395, doi: 10.1051/0004-6361:20078639
- Mastichiadis, A., & Kirk, J. G. 1997, *A&A*, 320, 19, doi: 10.48550/arXiv.astro-ph/9610058
- Mastichiadis, A., & Kirk, J. G. 2002, *Publications of the Astronomical Society of Australia*, 19, 138–142, doi: 10.1071/AS01108
- Narayan, R., & Piran, T. 2012, *MNRAS*, 420, 604, doi: 10.1111/j.1365-2966.2011.20069.x
- Padovani, P., & Giommi, P. 1995, *ApJ*, 444, 567, doi: 10.1086/175631
- Pandey, A., Gupta, A. C., & Wiita, P. J. 2017, *ApJ*, 841, 123, doi: 10.3847/1538-4357/aa705e
- . 2018, *ApJ*, 859, 49, doi: 10.3847/1538-4357/aabc5b
- Park, T., Kashyap, V. L., Siemiginowska, A., et al. 2006, *ApJ*, 652, 610, doi: 10.1086/507406
- Patel, S. R., Shukla, A., Chitnis, V. R., et al. 2018, *A&A*, 611, A44, doi: 10.1051/0004-6361/201731987
- Perlman, E. S., Stocke, J. T., Schachter, J. F., et al. 1996, *ApJS*, 104, 251, doi: 10.1086/192300
- Perlman, E. S., Madejski, G., Georganopoulos, M., et al. 2005, *ApJ*, 625, 727, doi: 10.1086/429688
- Pollack, M., Pauls, D., & Wiita, P. J. 2016, *ApJ*, 820, 12, doi: 10.3847/0004-637X/820/1/12
- Prince, R., Gupta, N., & Nalewajko, K. 2019, *ApJ*, 883, 137, doi: 10.3847/1538-4357/ab3afa
- Rodríguez-Pascual, P. M., Alloin, D., Clavel, J., et al. 1997, *ApJS*, 110, 9, doi: 10.1086/312996
- Rybicki, G. B., & Lightman, A. P. 1979, *Radiative processes in astrophysics*
- Scargle, J. D. 2020, *ApJ*, 895, 90, doi: 10.3847/1538-4357/ab8d38
- Shah, Z., Ezhikode, S. H., Misra, R., & Rajalakshmi, T. R. 2021, *MNRAS*, 504, 5485, doi: 10.1093/mnras/stab1244
- Shah, Z., Mankuzhiyil, N., Sinha, A., et al. 2018, *Research in Astronomy and Astrophysics*, 18, 141, doi: 10.1088/1674-4527/18/11/141
- Shah, Z., Misra, R., & Sinha, A. 2020, *MNRAS*, 496, 3348, doi: 10.1093/mnras/staa1746
- Sinha, A., Khatoun, R., Misra, R., et al. 2018, *MNRAS*, 480, L116, doi: 10.1093/mnrasl/sly136
- Sinha, A., Sahayanathan, S., Acharya, B. S., et al. 2017, *ApJ*, 836, 83, doi: 10.3847/1538-4357/836/1/83
- Sivakoff, G. R., Sarazin, C. L., & Carlin, J. L. 2004, *ApJ*, 617, 262, doi: 10.1086/425244
- Sokolov, A., Marscher, A. P., & McHardy, I. M. 2004, *ApJ*, 613, 725, doi: 10.1086/423165
- Stephens, M. A. 1977, *Biometrika*, 64, 583, doi: 10.1093/biomet/64.3.583
- Strüder, L., Briel, U., Dennerl, K., et al. 2001, *A&A*, 365, L18, doi: 10.1051/0004-6361:20000066
- Tagliaferri, G., Rivasio, M., Ghisellini, G., et al. 2003, *A&A*, 412, 711, doi: 10.1051/0004-6361:20034051
- Tramacere, A., Giommi, P., Perri, M., Verrecchia, F., & Tosti, G. 2009, *A&A*, 501, 879, doi: 10.1051/0004-6361/200810865
- Tramacere, A., Massaro, E., & Taylor, A. M. 2011, *ApJ*, 739, 66, doi: 10.1088/0004-637X/739/2/66
- Tramacere, A., Massaro, F., & Cavaliere, A. 2007, *A&A*, 466, 521, doi: 10.1051/0004-6361:20066723
- Urry, C. M., & Padovani, P. 1995, *PASP*, 107, 803, doi: 10.1086/133630
- Uttley, P., McHardy, I. M., & Vaughan, S. 2005, *MNRAS*, 359, 345, doi: 10.1111/j.1365-2966.2005.08886.x
- Valtonen, M. J., & Wiik, K. 2012, *MNRAS*, 421, 1861, doi: 10.1111/j.1365-2966.2011.20009.x
- van der Klis, M. 1989, *ARA&A*, 27, 517, doi: 10.1146/annurev.aa.27.090189.002505
- Vaughan, S. 2005, *A&A*, 431, 391, doi: 10.1051/0004-6361:20041453
- Vaughan, S., Edelson, R., Warwick, R. S., & Uttley, P. 2003a, *MNRAS*, 345, 1271, doi: 10.1046/j.1365-2966.2003.07042.x
- Vaughan, S., Fabian, A. C., & Nandra, K. 2003b, *MNRAS*, 339, 1237, doi: 10.1046/j.1365-8711.2003.06285.x
- Wagner, S. J., & Witzel, A. 1995, *ARA&A*, 33, 163, doi: 10.1146/annurev.aa.33.090195.001115
- Wang, Y., Xue, Y., Zhu, S., & Fan, J. 2018, *ApJ*, 867, 68, doi: 10.3847/1538-4357/aae307
- Wang, Y., Zhu, S., Xue, Y., et al. 2019, *ApJ*, 885, 8, doi: 10.3847/1538-4357/ab4416
- Wehrle, A. E., Carini, M., & Wiita, P. J. 2019, *ApJ*, 877, 151, doi: 10.3847/1538-4357/ab1b2d
- Yuan, Y. H., Fan, J. H., & Pan, H. J. 2015, *AJ*, 150, 67, doi: 10.1088/0004-6256/150/3/67
- Zhang, X. H., & Bao, G. 1991, *A&A*, 246, 21
- Zhang, Y. H., Treves, A., Celotti, A., et al. 2002, *ApJ*, 572, 762, doi: 10.1086/340349
- Zhang, Z., Gupta, A. C., Gaur, H., et al. 2021, *ApJ*, 909, 103, doi: 10.3847/1538-4357/abdd38